Nanostructured Bimetallic (Cu,Ni)/SiO_2 Catalysts for the Dehydrogenation of Ethanol Dehydrogenation to Acetaldehyde

Giovanni Pampararo[1], Gabriella Garbarino[2,3], Aliou Sadia Traoré[4], Ovidiu Ersen[4], Elena Spennati[2,3], Paola Riani[3,5], Guido Busca[2], Damien P. Debecker[1*]*

Corresponding authors: Damien.Debecker@uclouvain.be, Gabriella.Garbarino@unige.it

1. Université catholique de Louvain (UCLouvain), Institute of Condensed Matter and Nanosciences (IMCN), Place Louis Pasteur, 1, 1348 Louvain-la-Neuve, Belgium
2. University of Genova, DICCA, Department of Civil Chemical and Environmental Engineering, Via all'Opera Pia 15, 16145, Genova, Italy
3. INSTM, UdR di Genova, via Dodecaneso 31, 16146, Genova, Italy
4. Institut de Physique et de Chimie des Matériaux de Strasbourg (IPCMS), UMR 7504 Université de Strasbourg-CNRS, 23, Rue du Loess, 67200 Strasbourg, France.
5. University of Genova, DCCI, Department of Chemistry and Industrial Chemistry, Via Dodecaneso 31, 16146, Genova, Italy

Abstract:

Upgrading bioethanol to useful platform chemicals such as acetaldehyde requires the development of more effective and stable catalysts. In the non-oxidative dehydrogenation reaction, classically catalysed by Cu nanoparticles-based catalysts operating at relatively high temperatures under an inert atmosphere, deactivation usually proceeds through carbonaceous species deposition and active phase sintering. Herein, to improve the sintering resistance and to increase the catalytic activity at low temperature, we exploit the aerosol-assisted sol-gel process to prepare mesoporous bimetallic (Cu,Ni)/SiO_2 catalysts. The peculiar preparation method ensures a thorough dispersion of the metal(s) into the silica matrix before applying calcination that triggers metal exsolution and nanoparticles formation. Keeping the total metal loading constant (7.4 wt.%), we examine the influence of substituting Cu for Ni on the speciation of the metal nanoparticles. When the Ni loading is between 1.4% and 3.7 wt.%, Ni tends to segregate, forming Ni-enriched nanoparticles at the support surface. Cu species, instead, are partially embedded in the silica matrix. On the contrary, when the loading of Ni is low (0.1 wt.%), truly alloyed nanoparticles were formed, with an intimate mixing of the two metals. This last catalyst presented a remarkable acetaldehyde (AcA) productivity of 6.0 $g_{AcA}g_{cat}^{-1}h^{-1}$ and T = 673 K as compared to state-of-the-art benchmarks.

Keywords: nickel, copper, nanoparticles, mesoporous silica, bimetallic alloy, bioethanol, non-oxidative dehydrogenation, acetaldehyde.

1. INTRODUCTION

Biorefining is the concept of processing biomass feedstocks into a wide spectrum of valuable products [1]. The primary objective is to fully utilize biomass for the sustainable production of fuels, chemicals, and materials, while minimizing waste. Among the bio-based platform chemicals that can be effectively obtained from biomass feedstocks, bioethanol is particularly important, especially as a fuel source. While most bioethanol is still currently produced from corn (first-generation bioethanol), there is a growing trend toward producing bioethanol from lignocellulosic biomass (second-generation bioethanol). This shift is evidenced by the increasing production share, i.e. from 4% in 2018 to 13.4% in 2022. [2] However, beyond fuel applications, bioethanol conversion to other platform molecules is also a way to create value from biomass. [3,4]

Among these valuable platform chemicals, acetaldehyde stands out as it is employed as an intermediate in several market sectors such as the synthesis of maleic acid, acetic anhydride, peracetic acid, ethyl acetate, glyoxal, crotonaldehyde, pentaerythritol, mono-, di-, and trichloroacetyl chloride. [5] Today, most of the acetaldehyde is produced using a homogeneous $PdCl_2/CuCl_2$ catalyst, via the Wacker Hoechst process. [6] However, the use of a heterogeneous, thus recoverable and potentially reusable, catalyst is an attractive alternative. Converting bioethanol to acetaldehyde with heterogeneous catalysts can involve an oxidant, i.e., oxidative dehydrogenation, but it can also be carried out in an inert atmosphere, via the so-called "non-oxidative dehydrogenation" reaction. This endothermic reaction requires a metal-based catalyst to drive selectivity to the desired products. Catalysts based on Pd and Pt [7,8], Ag [9,10], Au [11,12], Co [13], ZnO [14], and Cu [15–17] have been reported as active catalysts for the non-oxidative dehydrogenation of ethanol.

Copper-based catalysts are extensively investigated because they were found to achieve high conversion rates while maintaining excellent selectivity to acetaldehyde (> 90%). This is related to the fact that Cu-based catalysts do not favour the over-oxidation of the produced acetaldehyde nor C-C cleavage to methane and CO_x. Nevertheless, rapid deactivation is still an unresolved challenge for this process. Both metal sintering and coking were reported to limit the catalyst lifetime. [18,19] Cu sintering causes a drop in active surface area and the exposure of the catalytically non-innocent support (e.g. alumina), with a consequent drop in acetaldehyde selectivity. Concomitantly, the formation of side products triggers catalyst fouling. Thus, to limit side reactions, silica can be employed as a relatively inert support for Cu nanoparticles, and Cu/SiO_2 catalysts have indeed been reported as highly selective to acetaldehyde. [20–22] Despite this, the design of deactivation-resistant catalysts that demonstrate both high activity levels and long-term stability is still demanded in this domain.

Leveraging on the aerosol-assisted sol-gel (AASG) preparation route (Scheme 1), [23] we recently disclosed the preparation of mesoporous Cu/SiO_2 catalysts, which showed good activity levels and high acetaldehyde selectivity. [24] However, because of the endothermic nature of the reaction, quite high temperatures (T> 573 K) are often needed to achieve valuable acetaldehyde productivity. These experimental conditions favour the formation of carbonaceous deposits and the sintering of the active phase that drastically reduce the catalyst stability over time.

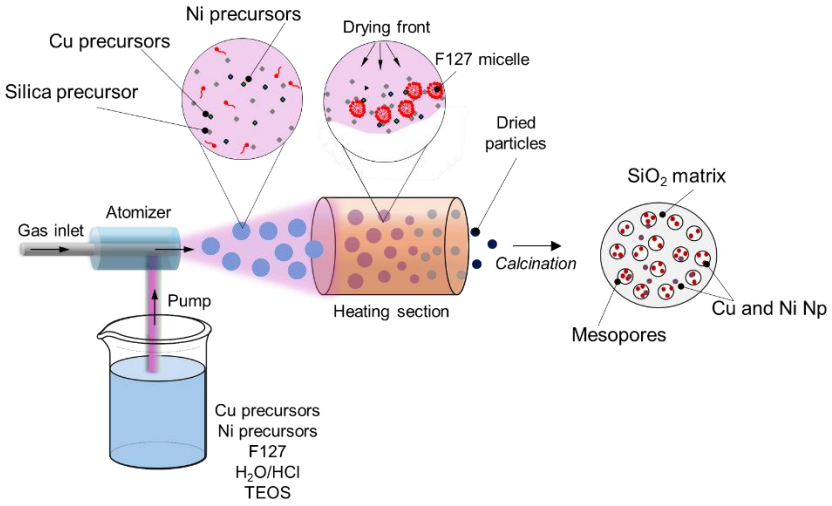

Scheme 1: Schematic view of the Aerosol Assisted Sol Gel (AASG) preparation process.

A possibility to minimize copper sintering and to increase the catalytic activity at lower temperatures is represented by the introduction of a second metal, with a higher thermal stability. In this perspective, nickel is often added to copper to form bimetallic catalysts. [25] In fact, Ni possesses a higher melting point (1728 K) as compared to Cu (1357 K). Furthermore, it has been argued that the introduction of nickel can lower the energy barrier for β C-H bond scission, [26,27] resulting in a reduction of the overall reaction activation energy in the ethanol dehydrogenation reaction. [28] Although alloying seems to be a straightforward method to increase thermal and catalytic performance of Cu based catalysts, it must be considered that i) thermal stability of metal alloys generally vary in a nonlinear way with composition [29] ii) alloying often also alter the chemical properties and hence the catalytic activity and/or selectivity of the catalyst. This effect strongly depends on the employed support, the synthesis method, and the studied reaction. [27,30]

The present work aims at exploiting the versatility of the AASG method to prepare bimetallic (Cu,Ni)-based catalysts in one step. The method offers a facile way to homogeneously disperse Ni and Cu precursors in mesoporous silica microspheres. Upon calcination, metal exsolution [31], nanoparticles formation, and metal alloying are expected to occur. Also, the strong interactions between the metal nanoparticle (NP) and the silica matrix from which they emerge could promote catalyst stability. With these tailored catalysts, we explore the effect of different Ni/Cu ratios on the physico-chemical properties of the catalysts and correlate them with ethanol dehydrogenation performance (activity, selectivity).

2. EXPERIMENTAL SECTION

2.1 *Catalysts preparation*

A first solution (solution A) was prepared by mixing 57 mL of ethanol (VWR, >99.8%), 8 mL of distilled water, and 3.88 g of Pluronic® F127 (Sigma Aldrich, ≃ 12600 g/mol). A second solution (solution B) was prepared by mixing 0.057 mol of TEOS (TCI Chemicals, >97.0%) with 0.548 mol of an aqueous HCl solution (20mL) at pH 2, made by diluting concentrated HCl (Roth, 37 wt.%). Both solutions were stirred overnight before being mixed. Just before spraying, $Cu(NO_3)_2 \cdot 2.5\ H_2O$

and/or $Ni(NO_3)_2 \cdot 6\ H_2O$ were added to achieve the desired Cu/Ni loadings. The resulting limpid solution was atomized using a TSI incorporated® atomizer at 30 psi (air pressure). The aerosol droplets were dried by passing through a quartz tube heated to 723 K by a tubular furnace. The dried material was collected on a 0.45 μm nitrocellulose filter (Sartorius, Stedim). The powders were calcined in a muffle furnace under static air, first at 623 K (60 K/h) for 3 hours, then at 823 K (60 K/h) for another 3 hours. The total theoretical metal loading was always 7.4 wt.% i.e. $(wt_{Metal}/(wt_{support} + wt_{Metal})) * 100$ %) and different ratios of Ni:Cu have been tested. Catalysts are denoted Ni_xCu_ySi where "A" stands for aerosol, and where "x" and "y" are the respective Cu and Ni weight loadings. Catalysts containing only Cu or Ni were also synthesized as references (Cu7.4Si and Ni7.4Si).

2.2 *Characterization techniques*

ICP-AES analyses were performed on an ICP Thermo Scientific 6500 instrument after dissolution of samples (≃100 mg) by Li metaborate-Li tetraborate fusion flux.

N_2-physisorption measurements were performed at 77 K using a Micrometrics Tristar 3000 instrument. Freshly calcined catalysts were degassed overnight at 443 K under vacuum before analysis. Specific surface area (SSA, m^2/g) was determined using the BET model in the relative pressure range of 0.05–0.30. Total pore volume (V_p) was estimated from the adsorption isotherm at $p/p_0 = 0.98$, and mesopore size distribution was calculated using the BJH model on the adsorption isotherms.

X-ray diffraction (XRD) analysis on fresh samples was conducted using a Bruker D8 Advance diffractometer configured in Bragg–Brentano geometry. This diffractometer utilized a Cu Kα radiation source (wavelength, $\lambda = 0.15418$ nm) operating at 1200 W (30 mA, 40 kV) over a 2θ range of 5°-100°. Measurements were taken with a step size of 0.05° (2θ) and 1.5 seconds per step. The Bruker Lynxeye XE-T detector was employed for detection. Powders were disposed on a Si wafer using a paraffin cream. Phase identification was achieved by consulting PCD Database. Some analyses were performed *in situ* under N_2 between 333 K and 573 K (step at 333 K, 473 K, 573 K) and then at 573 K for 30 min under a 10% V/V H_2/N_2 flow (~30 $mL \cdot min^{-1}$) The reactor chamber was an Anton Paar X.

On spent catalysts X-ray diffraction analysis was performed on a Rigaku SmartLab system, equipped with a 6 kW rotating Cu anode working at 40 kV and 150 mA and a D/teX Ultra one-dimensional silicon strip detector. The sample powders' measurements were carried out in air at room temperature using a zero-diffraction silicon substrate. Crystallites sizes of CuO and have been evaluated on the most intense peak by Scherrer formula, via DIFFRAC.EVA V4.2.1 software. Instrumental broadening has been considered. For CuO, peak at $2\theta = 35.66°$ has been considered. For NiO, peak at $2\theta = 43.29°$ has been considered.

UV-vis-NIR spectra were collected on a Jasco V-570 instrument in diffuse reflectance configuration.

A Zeiss SUPRA 40 VP Scanning Electron Microscope (FE-SEM) was used to study the morphology and composition of both fresh and spent catalysts. It features a high sensitivity "InLens" secondary electron detector and an OXFORD "INCA Energie 450 × 3" EDX spectrometer. Samples were

suspended in ethanol, and a drop of the mixture was placed on a Lacey Carbon copper grid for imaging after drying.
Scanning Transmission Electron Microscopy (STEM) analyses were carried out using a JEOL JEM-2100F microscope equipped with a spherical aberration probe corrector (Cs from CEOS) and operating at 200 kV. STEM micrographs were acquired using a camera length of 12 cm and with a probe size of 0.1 nm. Elemental analyses were carried out by energy dispersive X-ray spectroscopy (EDX) using a silicon drift detector (SDD) with a sensor size of 60 mm^2. In situ observations were performed using the Protochips Atmosphere system by environmental TEM. [32] The sample was placed in a closed cell composed of two micro-electro-mechanical system (MEMS) chips. This cell features a transparent SiNx window on both chips for electron observation and a SiC layer for increasing the temperature. [33] Observations are conducted at atmospheric pressure, with temperature ranging from room temperature to 773 K in a reducing environment of H_2/Ar (1:4) at a flow rate of 0.1 ml/min. The system was purged with argon before introducing the H_2/Ar gas mixture. To minimize electron damage and contamination, an electron dose below 10^{-5} $e \cdot nm^{-2} \cdot s^{-1}$ was used. Additionally, other areas not exposed to the electron beam were observed at different stages of the reduction process to compare with continuously exposed zones and to check for possible artefacts caused by the electron beam.

X-ray photoelectron spectroscopy (XPS) was performed at room temperature using an SSI-X-probe (SSX 100/206) spectrometer from Surface Science Instruments (USA), featuring a monochromatic Al K X-ray source (1486.6 eV). Samples were mounted on small holders with adhesive tape and placed on an insulating Macor® ceramic carousel. To reduce charge effects, a nickel grid was used over the samples, and an 8 eV flood gun was employed. The binding energy scale was calibrated using the Si 2p peak at 103.5 eV. Data was processed with CasaXPS software (UK), with spectral peaks deconvoluted into Gaussian and Lorentzian functions (85/15 ratio) after Shirley-type baseline subtraction.

BELCAT II Microtrac instrument, manufactured by BEL® (Japan), was used to perform Temperature-Programmed Reduction (TPR) analysis. 50 mg of catalyst was placed in a quartz tube, then, during the pre-treatment, the catalyst was heated to 393 K and maintained at this temperature for 30 minutes under a 75 mL/min argon (Ar) flow. Then, a gaseous mixture of 2% hydrogen (H_2) in argon (Ar) at a total flow of 75 mL/min was admitted to the reactor. At the same time, the temperature was increased from 393 K to 1073 K at a rate of 10 K/min. During each measurement, gases were properly calibrated for the quantification procedure.

2.4 *Catalytic activity evaluation*

The catalysts were tested in the ethanol dehydrogenation (and ethanol dehydration) reaction in a laboratory-scale microreactor using a fixed bed quartz tubular reactor loaded with 0.050 g of catalyst diluted in 0.450 g of commercial silica (Sigma-Aldrich), 60-70 mesh sieved. Prior reaction, the catalyst was pre-reduced in situ with 150 NmL/min of H_2-N_2 flow (20%-80% (v/v)) at 573 K for 30 min. The ethanol concentration was set at 2.4% (v/v) diluted in N_2 with a total flow rate of 120 NmL/min corresponding to GHSV (Gas Hourly Space Velocity, calculated with respect to the entire catalytic bed volume) of ~15000 h^{-1}. The oven temperature varied from 473 to 673 K with a temperature step of 50 K and kept for 45 minutes to ensure steady state conditions. The reaction products were analyzed with a gas chromatograph (GC) Agilent 4890 equipped with a Varian

capillary column "Molsieve 5A/Porabond A Tandem" and TCD and FID detectors in series and, for the identification of the compounds, with a gas chromatography coupled with mass spectroscopy (GC-MS) Thermo Scientific with TG-SQC column (15 m × 0.25 mm × 0.25 µm).

3. RESULTS AND DISCUSSION

3.1 Catalysts characterization

Elemental analyses by ICP-AES (Table 1) revealed a good agreement between effective and theoretical metal contents. However, a small but systematic discrepancy is observed, probably because of the hygroscopic nature of the metal precursors (nitrates).

Table 1: Composition and textural properties of catalysts. The last three columns represent, from left to right: i) the total amount of metal (mmol g^{-1} of catalyst), calculated from the ICP wt% values; ii) the total moles of metal (Ni and/or Cu) reduced by H_2 during the TPR experiment, which should closely match the ICP-derived metal content; and iii) the theoretical moles of metal expected, used to evaluate the quality of the synthesis.

Sample	Ni [wt.%[a]]	Cu [wt.%[a]]	SSA[b] [m^2/g]	V_p[c] [cm^3/g]	V_{micro} [d] [$cm^3 g^{-1}$]	D_p [e] [nm]	Amount of metal by ICP [$mmol_{tot}/g_{cat}$ [a]]	Amount of metal evaluated by TPR [$mmol_{tot}/g_{cat}$]	Theoretical amount of metal [$mmol_{tot}/g_{cat}$]
Cu7.4Si	/	6.73	460	0.53	0.10	8	1.06	1.02	1.18
Ni0.1Cu7.3Si	0.08	6.60	500	0.49	0.07	7	1.05	1.00	1.18
Ni0.9Cu6.5Si	0.81	5.54	450	0.50	0.11	6	1.01	0.97	1.21
Ni1.4Cu6.0Si	1.33	5.07	455	0.49	0.12	6	1.02	0.98	1.26
Ni3.7Cu3.7Si	3.17	2.96	460	0.51	0.06	5	1.01	1.00	1.16
Ni7.4Si	6.12	/	430	0.46	0.06	5	1.04	0.98	1.17

[a] evaluated by ICP-AES
[b] Specific Surface Area, determined by the BET method
[c] Total pore volume of pores, estimated from the adsorption branch of the isotherm at p/p_0=0.98.
[d] Microporous volume, estimated from the t-plot.
[e] Average mesopore diameter, estimated from the BJH model applied to the adsorption isotherms

N_2 adsorption−desorption isotherms are reported in Figure 1, and textural data are summarized in Table 1. For all the synthesized catalysts, irrespective of the Ni or Cu content, BET surface areas are similar, in the 430-500 m^2/g range. All catalysts exhibited Type IV isotherms, confirming the presence of mesopores. The hysteresis was of type H2 (asymmetrical with a steeper desorption branch than the adsorption one), suggesting a complex network of mesopores with restrictions. The forced closure of the hysteresis loop at p/p^0 values around 0.4 – 0.5 can be attributed to the tensile strength effect [34] and indicates the presence of mesopores (or pore entries) smaller than 3.8 nm. The nitrogen uptake at low relative pressure also indicates the presence of micropores whose contribution remains

minor (Table 1). Mesopore size distribution was always centred around a D_p of 6-10 nm, consistent with the use of the templating agent Pluronic F127. [35] The measured total pore volume was in the 0.46 – 0.53 cm^3/g range for all catalysts.

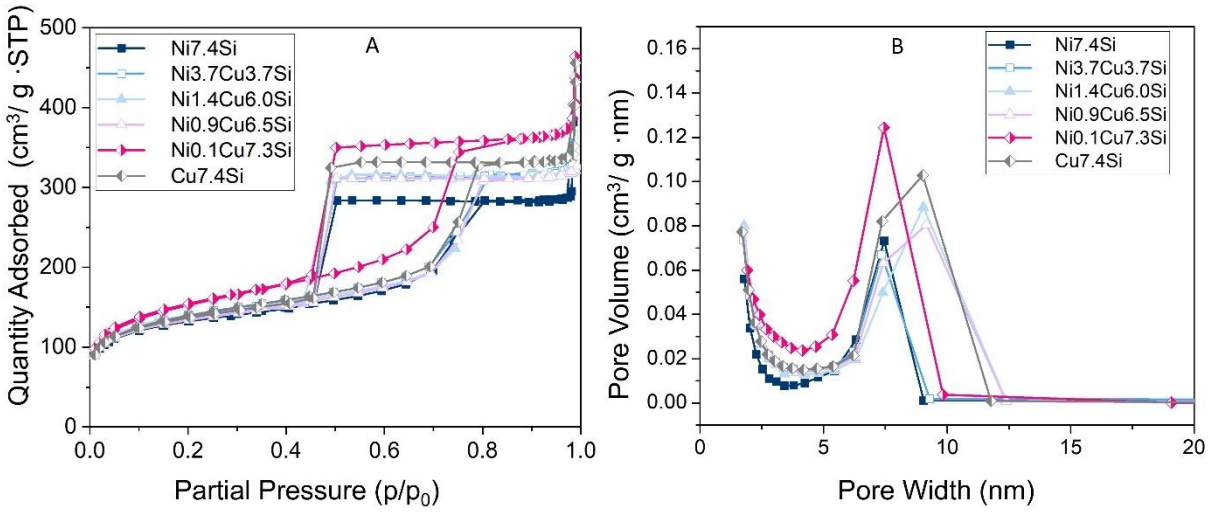

Figure 1: N_2 adsorption/desorption isotherms (panel A) and pore size distributions (panel B) on the investigated catalysts.

In XRD (Figure 2), a broad and weak signal around 2θ = 20° confirmed the amorphous nature of the silica support. [36] Diffraction peaks related to CuO (mS8, PCD No. 050661) were only detected for the catalysts with the highest proportion of Cu (Cu7.4Si and Ni0.1Cu7.3Si). Furthermore, only the two most intense peaks at 2θ = 35.7° and 38.5° were detectable. Average CuO crystallites size was estimated, via the Scherrer equation, to be roughly 8 nm. The diffraction pattern of Ni7.4Si showed two small and broad diffraction peaks at 2θ = 37° and 43.3°, attributable to NiO (cF8, PCD No. 1835670). Average crystal size was estimated to be roughly 6 nm. To sum up, XRD analysis revealed amorphous silica-based materials in which small CuO nanoparticles are detected in the Cu-rich samples and small NiO nanoparticles are detected in the Ni-based sample. In the catalysts with a more balanced Ni:Cu ratio, no metal oxide crystallites are detected. ~~suggesting a higher dispersion.~~

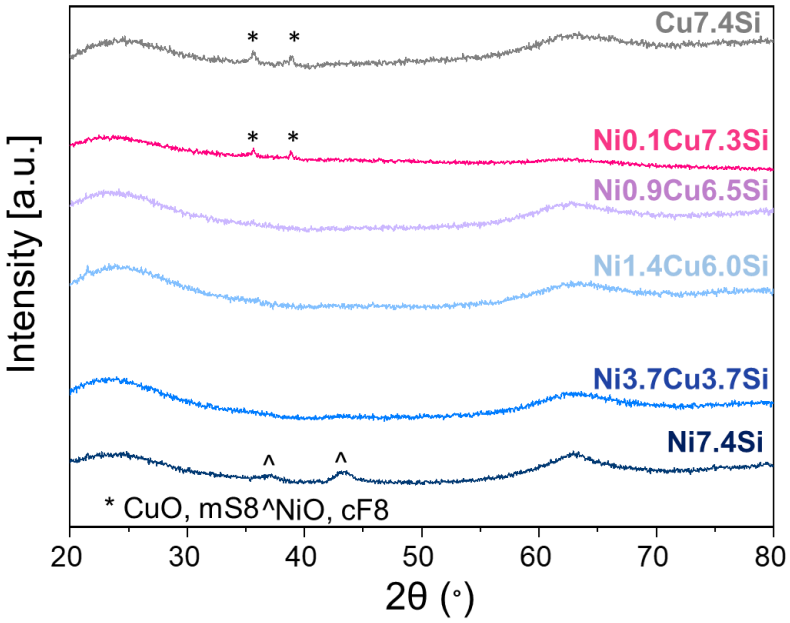

Figure 2: XRD patterns of the synthesized samples. The very broad peak at 2θ ≈ 63° is due to the presence of the fixing agent used in the sample preparation procedure for the analysis.

The microstructure of the catalysts was investigated by FE-SEM (ESI, Fig. S1). The material consisted of spherical particles, with a diameter ranging from 0.1 to 5 μm. TGA of the freshly prepared silica is reported (Figure S2) as a benchmark to show that the surfactant is fully removed at about 700 K, i.e. lower than calcination temperature (823 K) and no carbonaceous residues are present. The corresponding images did not reveal any strong contrast all over the spheres, suggesting a homogeneous distribution of the elements irrespective of the Ni and Cu loadings. Furthermore, via secondary electrons imaging, the high magnification microphotographs (Fig. S1, panels E, F) showed a wrinkled but homogeneous texture all over the spheres.

To further characterize morphology, texture, and metal distribution, (S)TEM analyses were conducted (Fig. 3). Mesopores, 5-10 nm in size, are visible in all samples, consistent with textural analyses. Elemental mapping further demonstrated that Cu and Ni species were homogeneously distributed over the support, regardless of their relative ratios. On Cu7.4Si, CuO nanoparticles were scarcely detected. As the Ni content increased, more metal oxide nanoparticles became visible outside the pores of the support spheres. Notably, in the Ni3.7Cu3.7Si catalyst, Ni-based nanoclusters were clearly detected on the external part of the silica sphere. This observation was further supported by a mass profile recorded over a detected bright particle (Fig. S3), which showed a higher Ni content compared to Cu. This phenomenon suggests that while low Ni loadings can be locally accommodated within the CuO structure, forming a mixed oxide phase, higher amounts (greater than 0.9 wt.%) lead to the preferential segregation of the two oxides, accordingly to the phase diagram of NiO-CuO.[37] Over Ni7.4Si catalyst, Ni-based nanoparticles were clearly visible, Statistical analysis of particle size distribution (Fig. S4) showed an average size of 3.6 ± 0.1 nm.

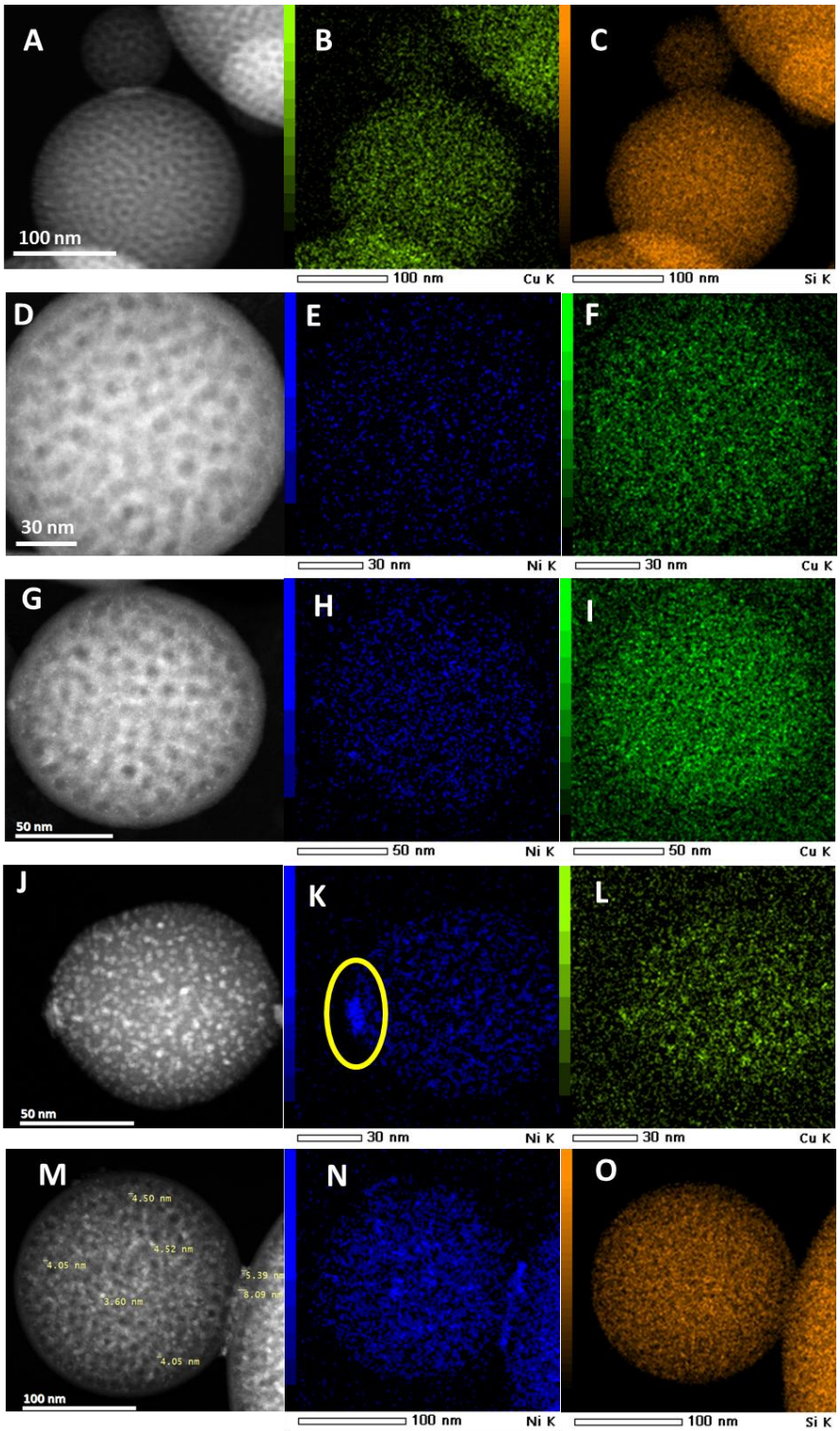

Figure 3: (S)TEM microphotographs of the investigated catalysts, panels A, B, C refer to Cu7.4Si. Panels D, E, F refer to Ni0.9Cu6.5Si; panels G, H, I refer to Ni1.4Cu6.0Si; panels J, K, L refer to Ni3.7Cu3.7Si, while panels M, N, O refer to Ni7.4Si. Panels A, D, G, J, M are acquired in dark-field mode. Images B, C, E, F, H, I, K, L, N, O refer to the elemental mapping. The yellow circle points out an ex-soluted nanoparticle.

To investigate the behavior of the catalysts in their reduced state, i.e. such as in catalytic conditions, environmental TEM analysis was performed on Ni3.7Cu3.7Si. This sample was selected based on the higher relative concentration of Ni over Cu previously observed in the ex-soluted nanoparticles.

When the catalyst was heated to 393 K under an inert atmosphere, the microstructure was preserved, revealing the presence of some metallic nanoparticles outside of the silica spheres (Fig. 4). However, after introduction of 20% v/v H_2/Ar at 558 K, new well-defined particles become visible at the surface of the spheres, as shown by the black arrows in Fig. 4. The formation of these particles, which can be even better observed at 750 K after 30 min (conditions that were used to mimic as much as possible the prereduction step before catalysis), indicating progressive exsolution of mainly Ni and then Cu (accordingly to mass profiles reported in Fig. S3).

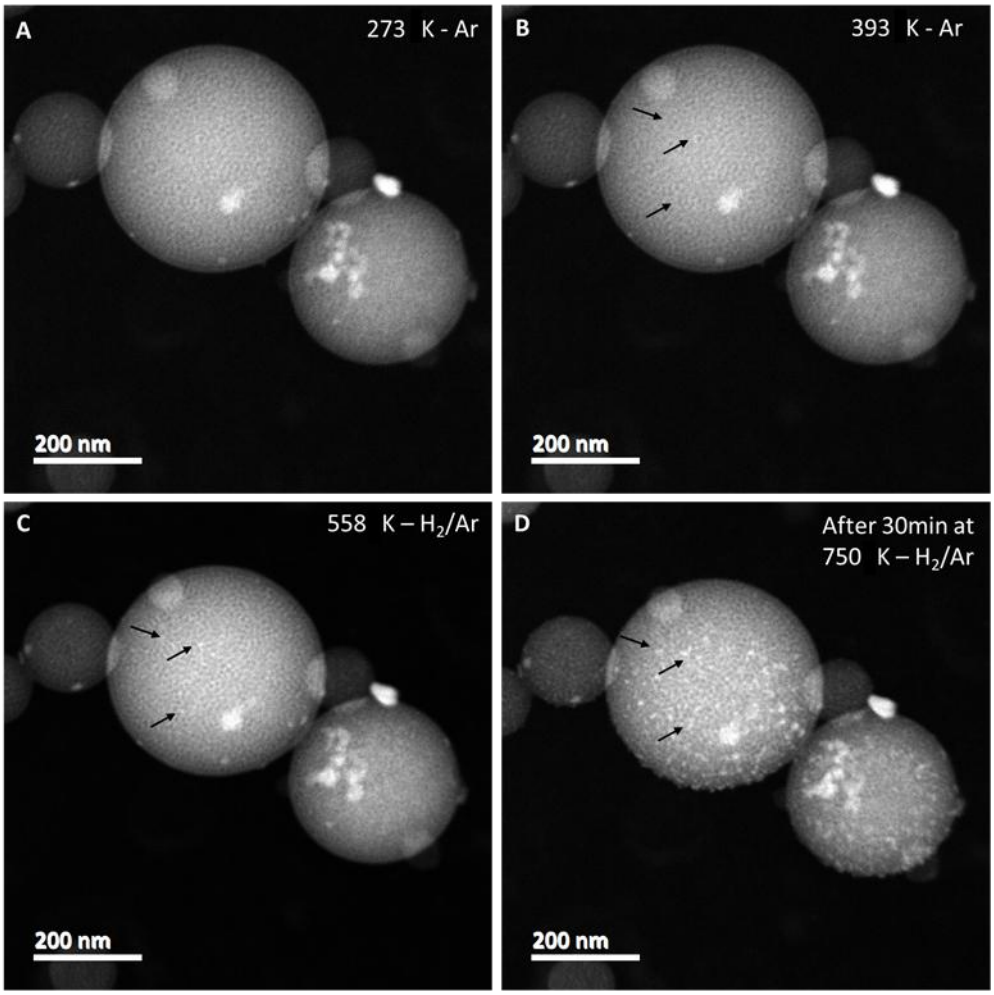

Figure 4: In situ monitoring by gas TEM of Ni3.7Cu3.7Si specimen. A) STEM HAADF image of a typical area of the sample at room temperature under Ar flow. B) STEM HAADF image of the same area at 393 K under Ar flow. C) STEM HAADF image immediately after the introduction of the H_2/Ar flow at 558 K. D) STEM HAADF image at 750 K, after maintaining the specimen for 30 min under H_2/Ar flow. Exsolution of the metal nanoparticles is highlighted by the appearance of bright spots all over the silica spheres indicated by the black arrows.

The UV-vis spectroscopy on the pristine silica did not present any absorption in the 240-1000 nm region (ESI, Fig. S5). The spectrum of the Cu7.4Si sample presented an absorption towards the lower wavenumber limit of the spectrometer, suggesting that it is due to an absorption edge around 260 nm, likely associated with the $O^{2-} \rightarrow Cu^{2+}$ charge transfer transition. Additionally, a band was observed with a maximum near 720 nm, which is likely due to dispersed Cu^{2+} ions (d-d transition). [38] However, a feature in the region below 700 nm may suggest that the absorption typical of CuO particles, with an edge above 800 nm, could also be present. [18] Thus, above-described data suggests that both CuO

particles and dispersed Cu^{2+} ions are present in the catalyst, in agreement with previously described results.[18,38]

The spectrum of Ni7.4Si is similar to the one previously reported for NiO/SiO_2. [39] It showed an absorption edge centered near 320 nm, due to $O^{2-} \rightarrow Ni^{2+}$ charge transfer transition, as well as d-d absorption bands centered at 423 nm and 734 nm, which are similar, although much broader than those reported for NiO. Besides, an absorption centered near 550 nm was also observable, likely due to dispersed Ni^{2+} ions, as previously discussed. [40] Thus, the spectrum suggests that small NiO particles are present together with dispersed Ni^{2+} ions in cation exchange sites.

The bimetallic samples showed a band centered in the 700-800 nm range, suggesting that an interaction between Ni and Cu ions exists, probably in the form of a mixed oxide phase, accordingly to the phase diagram of NiO-CuO.[37] The absorption near 425 nm, which would be indicative of a NiO phase, is evident in the Ni3.7Cu3.7Si sample but much less pronounced in Ni1.4Cu6.0Si and absent in Ni0.1Cu7.3Si. This indicates that NiO segregation occurred only markedly in Ni3.7Cu3.7Si, and, to a minor extent, in Ni1.4Cu6.0Si.

All in all, UV-vis data recalls the coexistence of bulk oxide nanoparticles (NiO, CuO) but also of Ni^{2+} and Cu^{2+} cations embedded in the support matrix. Moreover, distinct oxides seem to be formed only when Ni content is > 1.4 wt.%.

To investigate the reducibility of the catalysts H_2-TPR experiments were carried out (Fig. 5). The amounts of metal reduced by the TPR experiments are reported in Table 1. This amount is consistently ~15% lower than the theoretical $mmol_{tot}/g_{cat}$, which aligns with the discrepancy observed between ICP quantification and the theoretical values. In fact, in the whole range of metal loadings investigated here, the quantity of reduced metal closely approached the actual metal content measured by ICP (Fig. S6). This indicates that the Cu and Ni oxide species incorporated during synthesis are accessible to H_2 and can be quantitatively reduced to their metallic state.

The reduction profile (Fig. 5) can offer insights into the dispersion of metal species within the support, as well as into the interaction between the metal ions and the support. [41] In general, the stronger the interaction with the support, the higher the reduction temperature. In parallel, the reduction temperature depends on the nature of the oxide nanoparticles and their size. According to the literature [42,43], for CuO nanoparticles, the smaller the nanoparticle size, the lower the reduction temperature observed both in CO [42,43] and H_2 over not pre-reduced catalysts [42,43]. On the contrary, NiO nanoparticles exhibit an opposite behavior [44,45]: the smaller the nanoparticle size, the higher the reduction temperature.

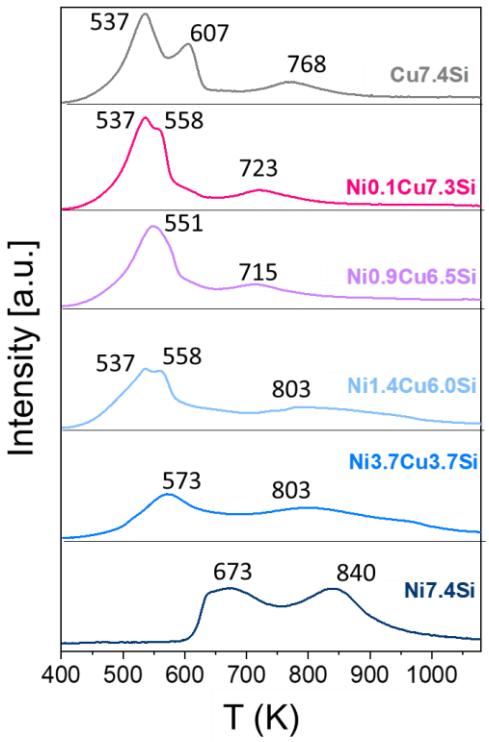

Figure 5: H_2-TPR profiles of the investigated catalysts.

In Cu7.4Si, copper oxide reduction began already at 473 K, reaching a first maximum at 537 K. This peak is the most intense, meaning that most of the smallest CuO nanoparticles are rapidly reduced. A second feature is observed at 607 K hinting at the presence of a portion of the copper oxide species that is less prone to reduction. This feature can be attributed either to larger nanoparticles of CuO or to CuO species presenting a stronger interaction with the silica matrix. A broad peak centered at 768 K was also observed, which is quite a high reduction temperature for copper oxide nanoparticles. Rather, this feature is tentatively attributed to copper (II) ions interacting with the silica matrix; such species were reported to be more difficult to reduce with respect to bare oxide nanoparticles dispersed over the support (as they first have to migrate, via exsolution, out of the silica walls). [46,47] The presence of such species matches well with i) previous studies regarding the adopted synthesis procedure (AASG) [24] and ii) the characterization techniques here reported, such as UV-vis, XPS, STEM, which show indeed the incorporation of Cu species within the silica matrix.

Over Ni7.4Si, two main reduction peaks were detected at 673 K and 840 K. The first peak can be attributed to the largest nanoparticles made of bulk nickel oxide, weakly interacting with the silica support. [48] Instead, the peak at 840 K could be related to smaller and hardly reducible NiO particles that are strongly interacting within the support. [49]

When introducing a small amount of Ni within Cu (i.e. Ni0.1Cu7.3), the same first peak at 537 K was detected, confirming the presence of small CuO nanoparticles. The second peak (607 K for Cu7.4Si) shifted to 558 K and 551 K, respectively. This means that Cu species were more easily reduced upon Ni introduction. Such effect agrees with i) the formation of a solid solution (i.e. an alloy), which is consistent with the reported solubility of NiO into CuO (up to 5% wt. of NiO can be incorporated into CuO structure[50]) and ii) the enhanced dissociation of H_2 with the doping of Ni into Cu. [50,51]

Besides, the reduction peak at 768 K was progressively shifted to 715 K, suggesting that Ni proximity enhances the reduction of these highly dispersed Cu(II) ions.
When the Ni loading was further increased (Ni0.9Cu6.5Si, Ni1.4Cu6.0Si, Ni3.7Cu3.7Si profiles), the first peak decreased due to the gradual disappearance of the smallest CuO nanoparticles. In contrast, the second peak (558–578 K) was attributed to the presence of larger and distinct Ni and Cu oxides. This is probably because CuO is no longer able to accommodate NiO. In the end, the broad peak at higher temperatures appeared to span a wider temperature range, likely due to the dispersion of both Cu(II) and Ni(II) species within the silica matrix.

To investigate the catalyst's surface, X-ray photoelectron spectroscopy (XPS) was carried out on the synthesized catalysts. Cu and Ni atomic concentrations were related to the respective concentrations obtained by ICP analyses and reported in Fig. 6. At 0.1 % and 1 % loading, Ni likely remains stable within the SiO_2 matrix, as the surface concentration matches the bulk concentration. At higher loadings, the Ni surface concentration markedly exceeds that of the bulk, indicating Ni exsolution to the surface of the microspheres.
For Cu, still at 3.7 wt.%, the bulk and surface Cu concentrations remain identical, suggesting that Cu is well incorporated within the SiO_2 matrix and exhibits higher solubility than Ni. At higher loadings, the surface Cu concentration unexpectedly decreases rather than increases. This behavior may be explained by either the direct formation of relatively large Cu particles on the surface giving rise to an inhomogeneous distribution of Cu on catalyst surface, or by the formation of small Cu nanoparticles that remain confined within the pores of the SiO_2 spheres, preventing their migration to the outer surface.
.

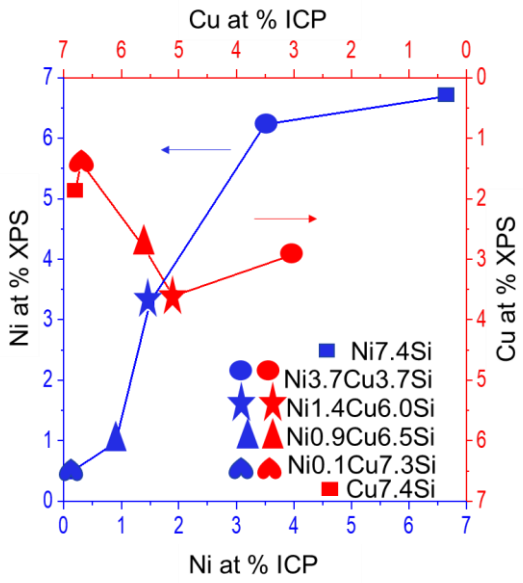

Figure 6: Correlation between Ni at% XPS and Ni at% ICP (blue), between Cu at% XPS and Cu at% ICP (red)

High resolution spectra for Cu 2p and Ni 2p peaks are reported in Fig. S7. Looking at the Cu $2p_{3/2}$ region of Cu7.4Si, three components were detected. A first one at 933 eV, a second one at about 935 eV, and the shake-up satellite peak (943 eV) evidenced the presence of Cu^{2+} species. The component at 933 eV and the satellite peak can be attributed to bulk-like CuO particles. [52] The component at higher binding energy (935 eV) could be attributed to the presence of Cu^{2+} species embedded in the

matrix (in good accord with TPR and UV-vis) [24]. In fact, this component progressively increased in intensity between Cu content of 3.7 wt.% and 6.5 wt.%, validating a partial but progressive dissolution of Cu species into the silica matrix.
The Ni $2p_{3/2}$ region featured a peak at ~853 eV and a shake-up satellite peak at ~862 eV. Similarly, Ni $2p_{1/2}$ region displayed two peaks at ~873 eV and ~879 eV, corresponding to the main and the satellite peaks, respectively. Interpretation of the Ni spectra features suggests that at the surface of Ni-based nanoparticles are mainly constituted of γ-NiOOH [53] rather than NiO. [54]
Overall, XPS analysis confirms that Ni species are uniformly distributed both in the bulk and on the surface, whereas Cu species tend to be more embedded, resulting in lower surface concentration.

3.2 Catalytic behavior

The catalysts were tested in the ethanol dehydrogenation reaction (Fig. 7). To prove the chemical inertness of the support, pristine (aerosol made) silica was first tested, and as expected, it exhibited no or negligible ethanol conversion (with no acetaldehyde production) between 150 K and 673 K (ESI, Fig. S8). Cu7.4Si (Fig. 7 A) showed a maximum ethanol conversion of 40 % at 573 K, after which the catalysts started to deactivate landing at ethanol conversion of 30 % at 673 K. The selectivity to acetaldehyde remained close to 100% in the whole range of tested temperature. Only above 623 K, traces of ethylene and diethyl ether were detected (yields <1%). With Ni7.4Si (Fig. 7 F) conversion was always lower, only kicking off significantly above 573 K (15 %) and landing at 38 % conversion at 673 K. Strikingly, the selectivity dropped rapidly as temperature increased; above 573 K, the main products were CH_4, CO and $C_2H_4 + C_2H_6$, with selectivity of 30.3 %, 38.7 % and 8.3 % at 673 K, respectively.
A completely different situation is found with the bimetallic catalysts. With the smallest percentage of Ni (Ni0.1Cu7.3Si, Fig. 7 B), ethanol conversion increased up to 93 % at 673 K, without any observable deactivation and keeping an acetaldehyde selectivity >95 %. Byproducts such as ethylene, propylene, methane, and CO were detected in negligible quantities, with a combined yield <4%. Ni0.9Cu6.5Si (Fig. 7 C) also shows high activity, reaching 80 % ethanol conversion at 673 K. However, acetaldehyde selectivity dropped down to 67 % at 673 K. Concomitantly, starting from 573 K, selectivity to CH_4+CO (with a 1:1 molar ratio), ethylene, and, to a lower extent, diethyl ether, progressively rose. Further increase in Ni loading led to a drastic change in the catalytic behavior of the bimetallic catalysts, clearly resembling that of Ni-based catalysts, i.e., promoting ethanol cracking to methane rather than dehydrogenation to acetaldehyde. In fact, the catalytic activity of Ni1.4Cu6.0Si (Fig. 7 D) and Ni3.7Cu3.7Si (Fig. 7 E) is similar, as ethanol conversion achieved 92 % for Ni1.4Cu6.0Si and 82 % for Ni3.7Cu3.7Si at 673 K, thus showing a decrease with increasing Ni content. While acetaldehyde selectivity was 88 % at 573 K, it dropped lower than 50 % at 673 K. Again, selectivity to CO and CH_4, with a near 1:1 ratio, increased progressively with the temperature increase.

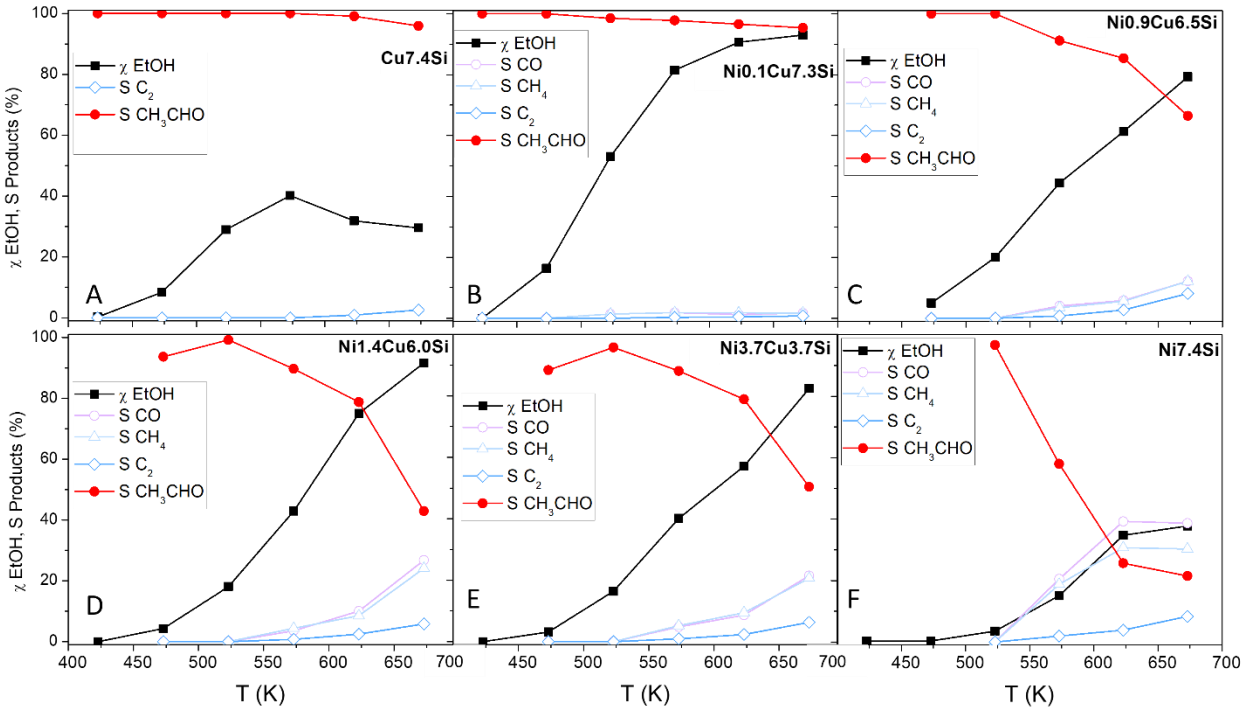

Figure 7: Catalytic behavior, in terms of ethanol conversion and product selectivity for all the synthesized catalysts (Panels A-F). Reaction conditions: 0.050 g of catalyst diluted in 0.450 g of commercial silica (Sigma-Aldrich), 60-70 mesh sieved. Ethanol concentration: 2.4% (v/v) diluted in N_2 with a total flow rate of 120 NmL/min. GHSV ~15000 h^{-1}.

To sum up, on the one hand Cu7.4Si presented almost total selectivity to acetaldehyde but had only moderate conversion and suffered from deactivation at high temperature. On the other hand, the Ni-based catalyst and bimetallic catalysts with relatively high Ni content showed high conversion but poor selectivity. Markedly standing out, the bimetallic catalyst with the lowest Ni content (0.1 wt.%), featured high conversion, which was maintained at high temperature, together with high selectivity at 673 K. The overall acetaldehyde yield reached by this catalyst was as high as 89 %, which roughly corresponds to a productivity of 6.0 $g_{AcA}.g_{cat}^{-1}.h^{-1}$.

Recently reported bimetallic Cu-Ni catalysts and Cu-SiO_2 catalysts are summarized in Table 2 for comparison. Most catalysts require low temperatures to maximize acetaldehyde selectivity and productivity except for the case of Ni1Cu10/MgAl, our catalyst was able to fully convert ethanol at high temperatures (i.e. 673 K) into acetaldehyde, achieving enhanced productivity (i.e. Productivity 2.5-15 times higher with respect to the reported benchmarks).

Table 2: Comparison of Acetaldehyde (AcA) Productivity with Cu-Ni and Cu based catalysts.

Sample	Cu [wt.%]	Ni [wt.%]	T [K]	WHSV [h^{-1}][a]	EtOH conversion [%]	Max AcA productivity [$g_{AcA}.g_{cat}^{-1}.h^{-1}$][b]
Ni0.1Cu7.3Si (this work)	7.3	0.1	673	7	93	6.0
Ni1Cu10/MgAl[55]	10	1	533	/[b]	40	17.44
NiCu alloy[56]	99.997	0.003	523	1.72	26.5	1.5

0.65%NiO–Cu–La_2O_3/Al_2O_3[57]	6	0.51	533	1.6	0.567	<0.4
Cu-Ni/γ-Al_2O_3[58]	0.8	0.4	573	0.5	0.61	<0.4
Cu-beta[59]	5	/	573	1	85	0.4
Cu-SiO_2[20]	2.13	/	528	4.73	65	2.8
Cu-SiO_2[60]	2.7	3.16	250	85	95	2.4

a: WHSV = mass flow rate of feed ($g \cdot h^{-1}$) / mass of catalyst (g)

b: productivity has been estimated by extrapolating data from the literature reported in the table

3.3 Spent catalysts characterization

The XRD patterns of the spent catalysts are shown in Fig. S9. In agreement with the reduction of NiO observed in the TPR between 673 and 840 K, Ni7.4Si did not exhibit any reflections corresponding to metallic nickel. Also, no metallic phase was detected in Ni3.7Cu3.7Si, suggesting that the few larger nanoparticles previously observed by STEM and environmental STEM in this catalyst are less prone to sintering. Instead, the metallic Cu (cF4) phase was identified in Ni0.9Cu6.5Si and Ni1.4Cu6.0Si, indicating that copper was reduced and likely underwent partial sintering during the test. Notably, contrasted behavior was highlighted in Ni0.1Cu7.3Si, where metallic phase reflections were barely distinguished. It should be noted that the XRD patterns of Ni0.1Cu7.3 were also evaluated under in-situ XRD conditions (Fig. S10) that mimicked the catalyst's pre-reaction thermal treatment, indicating that reduction occurred with only barely discernible peaks of the metallic phase after pre-reduction with hydrogen.

However, upon testing such catalysts for prolonged time on stream at 573 K, slow deactivation was observed (fig. S11). The spent catalyst presented diffraction peaks of metallic Cu (ESI, Fig. S12).

FE-SEM analyses were performed over spent catalysts (Fig. S13). The spent Ni1.4Cu6.0Si catalyst exhibited bright agglomerated crystallites easily detected also at the lowest magnifications. Such crystallites presented a metal content higher than the nominal value. In contrast, the micrographs of Ni0.1Cu7.3Si revealed a well-preserved catalyst microstructure, with only a few bright particles detected. Additionally, EDX analysis showed that the metal content is in quite good agreement with the nominal composition, suggesting at least for this specimen a minimal copper migration.

All in all, spent catalyst characterization confirmed the beneficial effect of alloying small percentages of Ni within Cu based catalysts to increase the thermal resistance under operating conditions.

3.4 Relationship between Ni and Cu mixing and the catalytic behavior

With the insights gained from catalysts characterization, we propose a unified correlation between the effect of mixing Ni and Cu in different ratios and the catalytic behavior in the ethanol non-oxidative dehydrogenation.

i) When there is only copper within silica (Cu7.4Si), after calcination, Cu species are made of bulk-like CuO nanoparticles with a size 3-10 nm and cationic copper species embedded into the silica matrix. This repartition can be explained by considering the synthesis process, where all the precursors are sprayed and atomized at the same time. Cu cations are initially trapped in the silica matrix and then, upon calcination, part of them remain embedded there and part of them undergoes exsolution to form CuO nanoparticles.

Characterization by UV-vis spectroscopy, STEM, H_2-TPR, and XPS converges towards this interpretation. In catalysis, after pre-reduction, Cu7.4Si presented almost total selectivity to acetaldehyde but suffered from rapid deactivation upon temperature increase. This can be due both to the deposition of carbonaceous species and to sintering related phenomena. [61,62] In fact, considering the former cause of deactivation, it has been reported that the Huttig temperature (at which surface atoms mobility starts) should already occur in the range 407 K ÷423 K. [63] This means that even at the lowest reaction temperatures, the smallest Cu nanoparticles may start to migrate, leading to a progressive and rapid coalescence when conditions approach the Tammann temperature (678 K).

ii) Over calcined Ni7.4Si, most of the nickel species are constituted by NiO (or oxy-hydroxide at the surface, as suggested by XPS) nanoparticles both weakly and strongly interacting with silica, depending on the size (TPR). STEM analysis showed that most of the supported nanoparticles were in the 4-9 nm range, preferring a surface arrangement on the external surface of the silica spheres. The catalytic behavior of monometallic Ni based catalysts was not favorable to ethanol dehydrogenation, rather catalyzing ethanol dehydration and cracking reactions.

iii) Bimetallic catalysts featuring relatively high Ni to Cu ratios (Ni0.9Cu6.5Si, Ni1.4Cu6.0Si, Ni3.7Cu3.7Si) led to a diversified situation in the oxide form, where, besides possible regions of mutual miscibility (formation of $Cu_{1-x}Ni_xO$), both NiO(OH) and CuO are formed as distinct phases. In fact, XPS and TPR analyses also suggested the formation of both the Ni and Cu oxides in the bulk state. Furthermore, STEM imaging revealed that most of the bright particles are primarily composed of Ni rather than Cu, indicating that Cu, more than Ni, tends to remain incorporated in silica. [21,64] In the end, even at the metallic state, beside regions where a true alloy (Cu,Ni,) was formed, the increase of Ni loading probably led to a lack of solubility [65–67] between the crystalline phases. Therefore, the system became less homogeneous. In catalysis, a competition between the dehydrogenation activity of the Cu-rich alloy regions and the cracking (to methane and CO) activity of Ni-rich alloy (or pure Nickel oxides nanoparticles) was observed.

iv) In the oxide form, when minimal quantities of Ni were added to the Cu catalyst (Ni0.1Cu7.3Si) a solid solution of the type $Cu_{1-x}Ni_xO$ is (at least partially) formed, as suggested with STEM and H_2-TPR experiments, thus ensuring a closeness between the two metals. At the metallic state, a (Cu,Ni) solid solution (i.e. an alloy) is more easily formed since metallic Ni and Cu have the same *fcc* crystalline structure and reciprocal solubilities have been already reported in literature.[68,69] The best catalyst in terms of ethanol conversion and acetaldehyde production was Ni0.1Cu7.3Si, reaching an acetaldehyde yield as high as 89 % at 673 K (Fig. 8), suggesting that the typical catalytic activity of copper was maintained even at the highest temperature. Characterization of the spent catalyst showed that alloy formation significantly reduced deactivation by coalescence in Ni0.1Cu7.3Si.

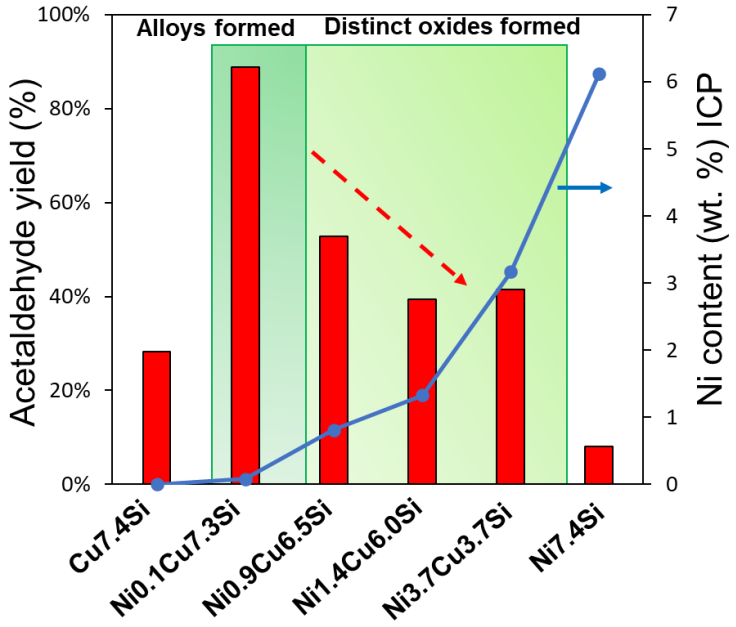

Figure 8: Correlation between the acetaldehyde yield at 673 K, the possible formation of truly (Cu,Ni) alloys and the Ni content evaluated by ICP analysis.

4 CONCLUSIONS

Bimetallic Cu-Ni catalysts have been successfully synthesized by the aerosol-assisted sol-gel method and tested in the ethanol non-oxidative dehydrogenation reaction to acetaldehyde. The impact of Ni was considered from both the perspective of structural modification and of its catalytic behavior.

When the Ni amount is between 0.9 wt. % and 3.7 wt. % bulk Cu species (CuO nanoparticles) and Ni species (NiOOH, NiO nanoparticles) are formed. Even though some minimal Ni is likely incorporated into the CuO matrix, the formation of two distinct oxidized phases is evidenced, leading to a heterogeneous enrichment of the two metals at the surface upon reduction processes. The main cause is probably the different behavior of Ni and Cu with the support. The former tends to be less akin to silica, while the latter tends to interact more intimately with silica. In catalysis, this heterogeneity is confirmed by the competition between the dehydrogenation activity of the Cu-rich alloy regions and the cracking (to methane and CO) activity of Ni-rich alloy (or pure nickel).

When Ni amount is 0.1 wt. %, under catalytic conditions (i.e. in the reduced form) a true solid-state solution, accordingly to the phase diagram of metallic Ni-Cu[69], is formed, meaning that Ni is fully hosted by Cu. This metal composition is favorable, at the same time, to an enhanced reducibility of copper and to a strengthening of its thermal stability. Indeed, the higher resistance of copper to coalescence, when minimal amounts of nickel are introduced, has been demonstrated through the analysis of the spent catalysts. Ultimately, Ni0.1Cu7.3Si exhibited superior catalytic activity compared to the other catalysts, maintaining nearly complete selectivity for acetaldehyde in the whole temperature range tested (423 K to 673 K). It achieved an acetaldehyde productivity of 6.0 $g_{AcA}.g_{cat}^{-1}.h^{-1}$ at 673 K, significantly outperforming (mono)metallic Cu7.4Si (1.9 $g_{AcA}.g_{cat}^{-1}.h^{-1}$) and Ni7.4Si (0.6 $g_{AcA}.g_{cat}^{-1}.h^{-1}$) and the other Cu- and/or Ni-based catalysts recently reported in the literature.

SUPPORTING INFORMATION

FE-SEM micrographs of as synthesized Ni1.4Cu6.0Si, Ni3.7Cu3.7Si, TEM micrograph of Ni3.7Cu3.7Si and relative mass profile, statistical analysis of particle size distribution over Ni7.3Si, DR-UV-VIS spectra of mono and bimetallic catalysts, correlation between total amount of metal reduced and the Ni content evaluated by ICP-AES, Cu 2p and Ni2p high resolution XPS spectra of the investigated catalysts, catalytic test for the bare support, XRD patterns of spent catalysts, FE-SEM images of spent Ni1.4Cu6.0Si and spent Ni0.1Cu7.3Si.

ACKNOWLEDGMENTS

GG and ES acknowledge the Project funded under the National Recovery and Resilience Plan (NRRP), Mission 4 Component 2 Investment 1.3 - Call for tender No. 1561 of 11. 10. 2022 of Ministero dell'Università e della Ricerca (MUR); funded by the European Union – NextGenerationEU,PE0000021, "Network 4 Energy Sustainable Transition – NEST".
GP acknowledges Fabio Lucaccioni for carrying out ICP analyses.

REFERENCES

(1) Conteratto, C.; Artuzo, F. D.; Benedetti Santos, O. I.; Talamini, E. Biorefinery: A Comprehensive Concept for the Sociotechnical Transition toward Bioeconomy. *Renew. Sustain. Energy Rev.* **2021**, *151*, 111527.

(2) *Home - ePURE*. https://www.epure.org/ (accessed 2025-12-04).

(3) Xiang, H.; Xin, R.; Prasongthum, N.; Natewong, P.; Sooknoi, T.; Wang, J.; Reubroycharoen, P.; Fan, X. Catalytic Conversion of Bioethanol to Value-Added Chemicals and Fuels: A Review. *Resour. Chem. Mater.* **2022**, *1* (1), 47–68.

(4) Pampararo, G.; Debecker, D. P. Bioethanol as a Sustainable Platform Molecule for the Synthesis of Chemical Commodities. *Reference Module in Chemistry, Molecular Sciences and Chemical Engineering* **2025**, 304–323.

(5) Eckert, M.; Fleischmann, G.; Jira, R.; Bolt, H. M.; Golka, K. Acetaldehyde. In *Ullmann's Encyclopedia of Industrial Chemistry*; Wiley-VCH Verlag GmbH & Co. KGaA: Weinheim, Germany, 2006.

(6) Fernandes, R. A.; Jha, A. K.; Kumar, P. Recent Advances in Wacker Oxidation: From Conventional to Modern Variants and Applications. *Catal Sci Technol* **2020**, *10* (22), 7448–7470.

(7) Amandusson, H.; Ekedahl, L. G.; Dannetun, H. Isotopic Study of Ethanol Dehydrogenation over a Palladium Membrane. *J Catal* **2000**, *195* (2), 376–382.

(8) Jalid, F.; Khan, T. S.; Haider, M. A. In-Silico Screening of Pt-Based Bimetallic Alloy Catalysts Using Ab Initio Microkinetic Modeling for Non-Oxidative Dehydrogenation of Ethanol to Produce Acetaldehyde. *MRS Commun* **2019**, *9* (1), 107–113.

(9) Sushkevich, V. L.; Ivanova, I. I.; Taarning, E. Mechanistic Study of Ethanol Dehydrogenation over Silica-Supported Silver. *ChemCatChem* **2013**, *5* (8), 2367–2373.

(10) Mamontov, G. V.; Grabchenko, M. V.; Sobolev, V. I.; Zaikovskii, V. I.; Vodyankina, O. V. Ethanol Dehydrogenation over Ag-CeO_2/SiO_2 Catalyst: Role of Ag-CeO_2 Interface. *Appl Catal A Gen* **2016**, *528*, 161–167.

(11) Molina, L. M.; Benito, A.; Alonso, J. A. Ab Initio Studies of Ethanol Dehydrogenation at Binary AuPd Nanocatalysts. *Mol. Catal.* **2018**, *449* (January), 8–13.

(12) Wang, C.; Garbarino, G.; Allard, L. F.; Wilson, F.; Busca, G.; Flytzani-Stephanopoulos, M. Low-Temperature Dehydrogenation of Ethanol on Atomically Dispersed Gold Supported on ZnZrOx. *ACS Catal* **2015**, *6* (1), 210–218.

(13) Rodriguez-Gomez, A.; Holgado, J. P.; Caballero, A. Cobalt Carbide Identified as Catalytic Site for the Dehydrogenation of Ethanol to Acetaldehyde. *ACS Catal* **2017**, *7* (8), 5243–5247.

(14) Ohira, M.; Liu, H.; He, D.; Hirata, Y.; Sano, M.; Suzuki, T.; Miyake, T. Catalytic Performance and Reaction Pathways of Cu/SiO_2 and ZnO/SiO_2 for Dehydrogenation of Ethanol to Acetaldehyde. *J. Jpn. Pet. Inst.* **2018**, *61* (4), 205–212.

(15) Phung, T. K. Copper-Based Catalysts for Ethanol Dehydrogenation and Dehydrogenative Coupling into Hydrogen, Acetaldehyde and Ethyl Acetate. *Int J Hydrogen Energy* **2022**, *47* (100), 42234–42249.

(16) Pang, J.; Yin, M.; Wu, P.; Li, X.; Li, H.; Zheng, M.; Zhang, T. Advances in Catalytic Dehydrogenation of Ethanol to Acetaldehyde. *Green Chem.* **2021**, *23* (20), 7902–7916.

(17) Huang, Y.; Wang, B.; Yuan, H.; Sun, Y.; Yang, D.; Cui, X.; Shi, F. The Catalytic Dehydrogenation of Ethanol by Heterogeneous Catalysts. *Catal Sci Technol* **2021**, *11* (5), 1652–1664.

(18) Pampararo, G.; Garbarino, G.; Riani, P.; Villa García, M.; Sánchez Escribano, V.; Busca, G. A Study of Ethanol Dehydrogenation to Acetaldehyde over Supported Copper Catalysts: Catalytic Activity, Deactivation and Regeneration. *Appl Catal A Gen* **2020**, *602* (June), 117710.

(19) Conesa, J. M.; Morales, M. V.; López-Olmos, C.; Rodríguez-Ramos, I.; Guerrero-Ruiz, A. Comparative Study of Cu, Ag and Ag-Cu Catalysts over Graphite in the Ethanol Dehydrogenation Reaction: Catalytic Activity, Deactivation and Regeneration. *Appl Catal A Gen* **2019**, *576*, 54–64.

(20) Pokorny, T.; Vykoukal, V.; Machac, P.; Moravec, Z.; Scotti, N.; Roupcova, P.; Karaskova, K.; Styskalik, A. Ethanol Dehydrogenation over Copper-Silica Catalysts: From Sub-Nanometer Clusters to 15 Nm Large Particles. *ACS Sustain Chem Eng* **2023**, *11* (30), 10980–10992.

(21) Xu, C.; Chen, G.; Zhao, Y.; Liu, P.; Duan, X.; Gu, L.; Fu, G.; Yuan, Y.; Zheng, N. Interfacing with Silica Boosts the Catalysis of Copper. *Nat Commun* **2018**, *9* (1), 1–10.

(22) Finger, P. H.; Osmari, T. A.; Cabral, N. M.; Bueno, J. M. C.; Gallo, J. M. R. Direct Synthesis of Cu Supported on Mesoporous Silica: Tailoring the Cu Loading and the Activity for Ethanol Dehydrogenation. *Catal Today* **2020**, No. August, 1–8.

(23) Debecker, D. P.; Le Bras, S.; Boissière, C.; Chaumonnot, A.; Sanchez, C. Aerosol Processing: A Wind of Innovation in the Field of Advanced Heterogeneous Catalysts. *Chem Soc Rev* **2018**, *47* (11), 4112–4155.

(24) Pampararo, G.; Garbarino, G.; Riani, P.; Vykoukal, V.; Busca, G.; Debecker, D. P. Ethanol Dehydrogenation to Acetaldehyde with Mesoporous Cu-SiO_2 Catalysts Prepared by Aerosol-Assisted Sol–Gel. *Chem. Eng. J.* **2023**, *465*, 142715.

(25) Cao, A.; Lu, R.; Veser, G. Stabilizing Metal Nanoparticles for Heterogeneous Catalysis. *Phys. Chem.* **2010**, *12* (41), 13499–13510.

(26) Wang, Q.; Duan, J. "Dawn"; Goetjen, T.; Hupp, J.; Notestein, J. Bimetallic NiCu Catalysts Supported on a Metal-Organic Framework for Non-Oxidative Ethanol Dehydrogenation. *J Catal* **2023**, *422*, 86–98.

(27) Shan, J.; Liu, J.; Li, M.; Lustig, S.; Lee, S.; Flytzani-Stephanopoulos, M. NiCu Single Atom Alloys Catalyze the CH Bond Activation in the Selective Non- Oxidative Ethanol Dehydrogenation Reaction. *Appl Catal B* **2018**, *226*, 534–543.

(28) Shan, J.; Janvelyan, N.; Li, H.; Liu, J.; Egle, T. M.; Ye, J.; Biener, M. M.; Biener, J.; Friend, C. M.; Flytzani-Stephanopoulos, M. Selective Non-Oxidative Dehydrogenation of Ethanol to Acetaldehyde and Hydrogen on Highly Dilute NiCu Alloys. *Appl Catal B* **2017**, *205*, 541–550.

(29) Porter, D. A.; Easterling, K. E.; Sherif, M. Y. Phase Transformations in Metals and Alloys, Fourth Edition. *Phase Transformations in Metals and Alloys, Fourth Edition* **2021**, 1–556.

(30) Feng, Y.; Shen, L.; Zhang, W.; Yuan, X.; Zhu, M.; Xu, J. Elucidating the Structure-Activity Relationship of the Bimetallic Ni-Cu Catalysts for CO_2 Hydrogenation. *J. CO_2 Util.* **2024**, *80*, 102683.

(31) Wintzheimer, S.; Luthardt, L.; Cao, K. L. A.; Imaz, I.; Maspoch, D.; Ogi, T.; Bück, A.; Debecker, D. P.; Faustini, M.; Mandel, K. Multifunctional, Hybrid Materials Design via Spray-Drying: Much More than Just Drying. *Adv. Mat.* **2023**, *35* (47), 2306648.

(32) *TEM Environmental Gas Cell: Atmosphere AX | Protochips*. https://www.protochips.com/solutions/in-situ-tem-solutions/in-situ-gas-cell/ (accessed 2024-07-02).

(33) Allard, L. F.; Bigelow, W. C.; Jose-Yacaman, M.; Nackashi, D. P.; Damiano, J.; Mick, S. E. A New MEMS-Based System for Ultra-High-Resolution Imaging at Elevated Temperatures. *Microsc Res Tech* **2009**, *72* (3), 208–215.

(34) Lai, W.; Yang, S.; Jiang, Y.; Zhao, F.; Li, Z.; Zaman, B.; Fayaz, M.; Li, X.; Chen, Y. Artefact Peaks of Pore Size Distributions Caused by Unclosed Sorption Isotherm and Tensile Strength Effect. *Adsorption* **2020**, *26* (4), 633–644.

(35) Paris, C.; Karelovic, A.; Manrique, R.; Bras, S. Le; Devred, F.; Vykoukal, V.; Styskalik, A.; Eloy, P.; Debecker, D. P. CO_2 Hydrogenation to Methanol with Ga- and Zn-Doped Mesoporous Cu/SiO2 Catalysts Prepared by the Aerosol-Assisted Sol-Gel Process. *ChemSusChem* **2020**, *13* (23), 6409–6417.

(36) Biswas, R. K.; Khan, P.; Mukherjee, S.; Mukhopadhyay, A. K.; Ghosh, J.; Muraleedharan, K. Study of Short Range Structure of Amorphous Silica from PDF Using Ag Radiation in Laboratory XRD System, RAMAN and NEXAFS. *J Non Cryst Solids* **2018**, *488*, 1–9.

(37) Delorme, C. L'asymétrie de l'ion Cuivre Bivalent Dans Des Combinaisons Du « type NaCl » et Du « type Spinelle ». I. Études Des Systèmes MO-CuO. *Bulletin de Minéralogie* **1958**, *81* (1), 19–28.

(38) Qiu, S. R.; Wood, B. C.; Ehrmann, P. R.; Demos, S. G.; Miller, P. E.; Schaffers, K. I.; Suratwala, T. I.; Brow, R. K. Origins of Optical Absorption Characteristics of Cu2+ Complexes in Aqueous Solutions. *Phys. Chem.* **2015**, *17* (29), 18913–18923.

(39) Riani, P.; Spennati, E.; Garcia, M. V.; Escribano, V. S.; Busca, G.; Garbarino, G. Ni/Al2O3 Catalysts for CO_2 Methanation: Effect of Silica and Nickel Loading. *Int J Hydrogen Energy* **2023**, *48* (64), 24976–24995.

(40) Bonneviot, L.; Legendre, O.; Kermarec, M.; Olivier, D.; Che, M. Characterization by UV-Vis-NIR Reflectance Spectroscopy of the Exchange Sites of Nickel on Silica. *J Colloid Interface Sci* **1990**, *134* (2), 534–547.

(41) Van Der Grift, C. J. G.; Mulder, A.; Geus, J. W. Characterization of Silica-Supported Copper Catalysts by Means of Temperature-Programmed Reduction. *Appl Catal* **1990**, *60* (1), 181–192.

(42) Zedan, A. F.; Mohamed, A. T.; El-Shall, M. S.; Alqaradawi, S. Y.; Aljaber, A. S. Tailoring the Reducibility and Catalytic Activity of CuO Nanoparticles for Low Temperature CO Oxidation. *RSC Adv* **2018**, *8* (35), 19499–19511.

(43) Jackson, S. D.; Robertson, F. J.; Willis, J. A Study of Copper/Silica Catalysts: Reduction, Adsorption and Reaction. *J. Mol. Catal.* **1990**, *63* (2), 255–268.

(44) Fedorov, A. V.; Kukushkin, R. G.; Yeletsky, P. M.; Bulavchenko, O. A.; Chesalov, Y. A.; Yakovlev, V. A. Temperature-Programmed Reduction of Model CuO, NiO and Mixed CuO–NiO Catalysts with Hydrogen. *J Alloys Compd* **2020**, *844*, 156135.

(45) Villarroel-Rocha, J.; Gil, A. Modeling the Temperature-Programmed Reduction of Metal Oxide Catalysts by Considering the Particle-Size Distribution Effect. *Chem. Eng. J.* **2024**, *487*, 150722.

(46) Wendlandt, K. P.; Vogt, F.; Mörke, W.; Achkar, I. A Comparative Study of State and Reactivity of Copper Ions Embedded in Various Molecular Sieve Materials. *Stud Surf Sci Catal* **1991**, *69* (C), 223–230.

(47) Tohidi, S. H.; Gholamzadeh, S.; Shirazi, M. A. Z.; Novinrooz, A. J. Characterization of Sol–Gel Derived CuO/SiO2 Nanostructure on Temperature. *Int. J. Ind. Chem.* **2014**, *5* (3–4), 63–68.

(48) Mile, B.; Stirling, D.; Zammitt, M. A.; Lovell, A.; Webb, M. The Location of Nickel Oxide and Nickel in Silica-Supported Catalysts: Two Forms of "NiO" and the Assignment of Temperature-Programmed Reduction Profiles. *J Catal* **1988**, *114* (2), 217–229.

(49) Drobná, H.; Kout, M.; Sołtysek, A.; González-Delacruz, V. M.; Caballero, A.; Čapek, L. Analysis of Ni Species Formed on Zeolites, Mesoporous Silica and Alumina Supports and Their Catalytic Behavior in the Dry Reforming of Methane. *React. Kinet. Mech. Catal.* **2017**, *121* (1), 255–274.

(50) Robertson, S. D.; McNicol, B. D.; De Baas, J. H.; Kloet, S. C.; Jenkins, J. W. Determination of Reducibility and Identification of Alloying in Copper-Nickel-on-Silica Catalysts by Temperature-Programmed Reduction. *J Catal* **1975**, *37* (3), 424–431.

(51) Xiao, T.; Xie, J.; Cheng, J.; Dai, X.; Lu, S.; Zuo, R.; Li, Z.; Yang, Z. Al_2O_3 Supported NiCu Alloy as a Stable Catalyst for Selective Hydrogenation of Phthalic Anhydride to Phthalide. *Appl Catal A Gen* **2023**, *660*, 119189.

(52) Biesinger, M. C. Advanced Analysis of Copper X-Ray Photoelectron Spectra. *Surf. Interface Anal.* **2017**, *49* (13), 1325–1334.

(53) Hu, C. W.; Yamada, Y.; Yoshimura, K. Fabrication of Nickel Oxyhydroxide/Palladium (NiOOH/Pd) Thin Films for Gasochromic Application. *J Mater Chem C Mater* **2016**, *4* (23), 5390–5397.

(54) Bagus, P. S.; Nelin, C. J.; Brundle, C. R.; Crist, B. V.; Ilton, E. S.; Lahiri, N.; Rosso, K. M. Main and Satellite Features in the Ni 2p XPS of NiO. *Inorg Chem* **2022**, *61* (45), 18077–18094.

(55) De Waele, J.; Galvita, V. V.; Poelman, H.; Gabrovska, M.; Nikolova, D.; Damyanova, S.; Thybaut, J. W. Ethanol Dehydrogenation over Cu Catalysts Promoted with Ni: Stability Control. *Appl Catal A Gen* **2020**, *591*, 117401.

(56) Shan, J.; Janvelyan, N.; Li, H.; Liu, J.; Egle, T. M.; Ye, J.; Biener, M. M.; Biener, J.; Friend, C. M.; Flytzani-Stephanopoulos, M. Selective Non-Oxidative Dehydrogenation of Ethanol to Acetaldehyde and Hydrogen on Highly Dilute NiCu Alloys. *Appl Catal B* **2017**, *205*, 541–550.

(57) He, J.; Li, X.; Kou, J.; Tao, T.; Shen, X.; Jiang, D.; Lin, L.; Li, X. Catalytic Upgrading of Ethanol to Higher Alcohols over Nickel-Modified Cu–La_2O_3 /Al_2O_3 Catalysts. *Catal Sci Technol* **2023**, *13* (1), 170–177.

(58) Yergaziyeva, G. Y.; Dossumov, K.; Mambetova, M. M.; Strizhak, P. Y.; Kurokawa, H.; Baizhomartov, B. Effect of Ni, La, and Ce Oxides on a Cu/Al_2O_3 Catalyst with Low Copper Loading for Ethanol Non-Oxidative Dehydrogenation. *Chem Eng Technol* **2021**, *44* (10), 1890–1899.

(59) Yu, D.; Dai, W.; Wu, G.; Guan, N.; Li, L. Stabilizing Copper Species Using Zeolite for Ethanol Catalytic Dehydrogenation to Acetaldehyde. *Chin. J. Catal.* **2019**, *40* (9), 1375–1384.

(60) Zhang, H.; Tan, H. R.; Jaenicke, S.; Chuah, G. K. Highly Efficient and Robust Cu Catalyst for Non-Oxidative Dehydrogenation of Ethanol to Acetaldehyde and Hydrogen. *J Catal* **2020**, *389*, 19–28.

(61) Vogt, E. T. C.; Fu, D.; Weckhuysen, B. M. Carbon Deposit Analysis in Catalyst Deactivation, Regeneration, and Rejuvenation. *Angew. Chem. Int. Ed.* **2023**, *62* (29), e202300319.

(62) Pampararo, G.; Hlavenková, Z.; Styskalik, A.; Debecker, D. P. Suppressing On-Stream Deactivation of $CuSiO_2$ Catalysts in the Dehydrogenation of Bioethanol to Acetaldehyde. *Catal Sci Technol* **2024**, *14* (17), 4912–4926.

(63) Moulijn, J. A.; Van Diepen, A. E.; Kapteijn, F. Catalyst Deactivation: Is It Predictable?: What to Do? *Appl Catal A Gen* **2001**, *212* (1–2), 3–16.

(64) van Deelen, T. W.; Hernández Mejía, C.; de Jong, K. P. Control of Metal-Support Interactions in Heterogeneous Catalysts to Enhance Activity and Selectivity. *Nat. Catal.* **2019**, *2* (11), 955–970.

(65) Turchanin, M. A.; Agraval, P. G.; Abdulov, A. R. Phase Equilibria and Thermodynamics of Binary Copper Systems with 3d-Metals. VI. Copper-Nickel System. *Powder Metall. Met. Ceram.*, **207,** *46* (9–10), 467–477.

(66) Guisbiers, G.; Khanal, S.; Ruiz-Zepeda, F.; Roque De La Puente, J.; José-Yacaman, M. Cu–Ni Nano-Alloy: Mixed, Core–Shell or Janus Nano-Particle? *Nanoscale* **2014**, *6* (24), 14630–14635.

(67) Ferrando, R.; Jellinek, J.; Johnston, R. L. Nanoalloys: From Theory to Applications of Alloy Clusters and Nanoparticles. *Chem Rev* **2008**, *108* (3), 845–910.

(68) Komal, N.; Ali, G.; Sohail, M.; Mazhar, M.; Malik, Z.; Wattoo, M. H. S. Facile Preparation of Porous Cu, Ni, and Cu–Ni Alloy as Electrodes for Supercapacitor Application. *Mater Chem Phys* **2023**, *295*, 127060.

(69) Marenych, O.; Kostryzhev, A. Strengthening Mechanisms in Nickel-Copper Alloys: A Review. *Metals 2020, Vol. 10, Page 1358* **2020**, *10* (10), 1358.

TOC

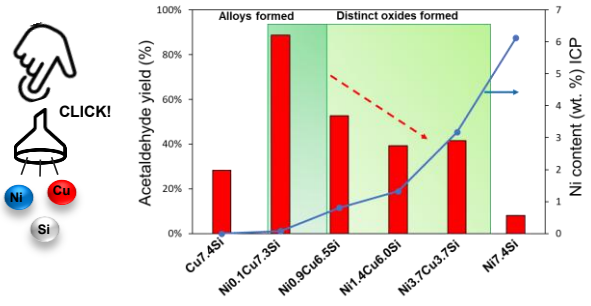
CLICK!
Ni
Cu
Si
Alloys formed
Distinct oxides formed
Acetaldehyde yield (%)
Ni content (wt. %) ICP
100%
80%
60%
40%
20%
0%
7
6
5
4
3
2
1
0
Cu7.4Si
Ni0.1Cu7.3Si
Ni0.9Cu6.5Si
Ni1.4Cu6.0Si
Ni3.7Cu3.7Si
Ni7.4Si